Epitaxial short-period PbTiO_{3}/BiFeO_{3} superlattices studied by first-principles calculations

Yurong Yang, Massimiliano Stengel, Wei Ren, X. H. Yan, and L. Bellaiche

Phys. Rev. B **86**, 144114 — Published 23 October 2012

DOI: 10.1103/PhysRevB.86.144114

Original phenomena in epitaxial $PbTiO_3/BiFeO_3$ superlattices from first principles

Yurong Yang[1,2], Massimiliano Stengel[3,4], Wei Ren[1,5], X. H. Yan[2,6] and L. Bellaiche[1]

[1]*Physics Department and Institute for Nanoscience and Engineering, University of Arkansas, Fayetteville, Arkansas 72701, USA*

[2]*Physics Department, Nanjing University of Aeronautics and Astronautics, Nanjing 210016, China*

[3]*Institut de Ciència de Materials de Barcelona (ICMAB-CSIC), Campus UAB, 08193 Bellaterra, Spain*

[4]*ICREA - Institució Catalana de Recerca i Estudis Avançats, ES-08010 Barcelona, Spain*

[5]*Department of Physics, Shanghai University, 99 Shangda Road, Shanghai 200444, China*

[6]*College of Electronic Science and Engeering, Nanjing University of Posts and Telecommunication, Nanjing 210003,China*

Abstract

First-principles calculations are used to predict properties of (001) epitaxial, short-period $PbTiO_3/BiFeO_3$ superlattices (SL) as a function of the in-plane lattice constant. These heterostructures exhibit original phenomena, such as three strain-driven isostructural phase transitions (two being of first-order and one being of second-order); five equilibrium phases that all differ in symmetry from those found in the pure $PbTiO_3$ (PTO) and $BiFeO_3$ (BFO) films; and the presence of significant oxygen octahedra tiltings in the PTO layers of the superlattice within a broad range of epitaxial strain values. All these unusual features can be understood from (i) the knowledge of the corresponding phases in the pure PTO and BFO films; (ii) the requirement that the out-of-plane component of the "formal" polarization (including ferroelectric and compositional dipoles) be homogeneous inside the superlattice; and (iii) the competition between polarization and oxygen octahedral tilting, in presence of electrostatic couplings and interfacial proximity effects.

PACS numbers: 77.55.Nv, 61.50.Ks, 68.65.Cd, 77.80.bn

I. INTRODUCTION

Various original phenomena have been recently reported in multiferroic $BiFeO_3$ (BFO) thin films under compressive or tensile strains. For instance, transitions towards states with giant axial ratio and polarization[1,2], accompanied by an enhancement of magnetoelectric coefficients[3,4], have been discovered in these systems. Other examples include a photovoltaic effect[5,6], an anomalous dependency of critical temperatures with misfit strain[7] and the nearly simultaneous occurrence of a ferroelectric and a magnetic transition near room temperature[8,9] in (001) BFO films. Interpenetrated arrays of vortices and antivortices resulting from a pure gyrotropic phase transition have also been predicted to occur in epitaxial (110) $BiFeO_3$ systems[10].

Another active research topic involving BFO and having the potential to lead to novel effects consists in investigating heterostructures made by mixing $BiFeO_3$ with another material. For instance, suppression of leakage current has been seen in $BiFeO_3/LaNiO_3$[11] and $BiFeO_3/SrTiO_3$ superlattices[12], magnetostructural effect has been predicted in a $BiFeO_3/BiMnO_3$ checkerboard heterostructure[13], and an antiferrodistortive phase transition has been observed at the $BiFeO_3/La_{0.7}Sr_{0.3}MnO_3$ interface[14].

Based on all these recent findings, it is natural to wonder if varying the misfit strain (within a reasonably large window) in an heterostructure containing BFO can further result in the discovery of original effects – especially, when realizing that multilayer oxide heterostructures have been shown to possess unexpected phenomena such as an interface-mediated conduction[15], superconductivity[16], multiferroic effect[17], and improper ferroelectricity[18].

The aim of this manuscript is to demonstrate that particular BFO heterostructures, namely short-period superlattices consisting of alternating $BiFeO_3$ layers with $PbTiO_3$ (PTO) layers, have indeed surprises in store when varying the misift strain. For instance, they undergo three isostructural transitions and possess characteristics that are quantitatively but also qualitatively different than those existing in the corresponding pure BFO and PTO films for the same in-plane lattice constants. Our first-principle-based computation further reveals the origins of such unusual features.

The paper is organized as follows. In Sec.II, we report computational details, introduce electrostatic analysis, and indicate the cell-by-cell decomposition of oxygen octahedra tilts in

the investigated superlattices. In particular, the distinction between *formal* (total), *built-in* (non-switchable) and *effective* (ferroelectric) polarization is documented in Section II. Results for pure PTO, BFO, and PTO/BFO superlattices under epitaxial strain are provided and discussed in length in Section III. Finally, a summary and conclusions are given in Section IV.

II. THEORY

A. Computational methods

Here, density-functional calculations within the local spin density approximation (LSDA) plus the Hubbard parameter U (with U=3.8 eV for Fe ions[19,20]) are performed, using the Vienna ab initio simulation package (VASP)[21]. Five different (001) *epitaxial* films are considered: pure $PbTiO_3$, pure $BiFeO_3$, and three short-period $[PbTiO_3]_n/[BiFeO_3]_n$ ($[PTO]_n/[BFO]_n$) superlattices ($n = 1, 2, 3$), where PTO and BFO layers alternate along the pseudo-cubic [001] direction. An example of the superlattice (SL) corresponding to $n = 3$ is shown in Fig. 1(a). Their in-plane lattice vectors are: $\mathbf{a_1} = 2a_{\rm IP}\mathbf{x}$ and $\mathbf{a_2} = 2a_{\rm IP}\mathbf{y}$, where $a_{\rm IP}$ is the in-plane lattice constant and where $\mathbf{x}$ and $\mathbf{y}$ are unit vectors along the x- and y-axis, respectively (that lie along the pseudo-cubic [100] and [010] directions, respectively). The third lattice vector is defined by $\mathbf{a_3} = a_{\rm IP}(\delta_1\mathbf{x} + \delta_{\mathbf{2}}\mathbf{y} + (\mathbf{2}n + \delta_{\mathbf{3}})\mathbf{z})$ for the investigated $[PTO]_n/[BFO]_n$ superlattices *versus* $\mathbf{a_3} = a_{\rm IP}(\delta_1\mathbf{x} + \delta_{\mathbf{2}}\mathbf{y} + (\mathbf{2} + \delta_{\mathbf{3}})\mathbf{z})$ for PTO and BFO films – where $\mathbf{z}$ is the unit vector along the out-of-plane, [001] direction. The supercells used to study PTO, BFO and $[PTO]_1/[BFO]_1$ therefore all contains 40 atoms, while those used to model $[PTO]_2/[BFO]_2$ and $[PTO]_3/[BFO]_3$ possess 80 and 120 atoms, respectively. For any considered $a_{\rm IP}$, the δ_1, δ_2 and δ_3 variables and the atomic positions are relaxed to minimize the total energy, Hellman-Feynman forces and the σ_3, σ_4 and σ_5 components of the stress tensor – in order to mimic perfect (001) epitaxy. The axial ratio of the resulting structure is provided by $1 + \frac{\delta_3}{2n}$ for the $[PTO]_n/[BFO]_n$ superlattices and by $1 + \frac{\delta_3}{2}$ for pure PTO and BFO epitaxial films. The projected augmented wave method and an energy cutoff of 550 eV are employed. A $3\times3\times m$ k-point mesh is used for the $[PTO]_n/[BFO]_n$ SL with $m = 3, 2, 1$ when $n = 1, 2, 3$, respectively, while a k-point mesh of $3\times3\times3$ is used for pure PTO and BFO films. Fe ions that are next nearest neighbors of each other are imposed to have opposite

magnetic moments in both the studied BFO system and the considered superlattices – as consistent with the G-type antiferromagnetism existing in BFO films[22]. The space group of the different structures reported in this manuscript are determined from the "FINDSYM" and "BPLOT"[23] softwares.

B. Electrostatic analysis

The *total* polarization $\tilde{\mathbf{P}}$ of each supercell configuration is calculated by first mapping the electronic density onto a system of classical point charges, by means of a Wannier transformation (the Wannier functions are calculated using the Wannier90 code[24], together with the VASP simulation package[21]). Then, $\tilde{\mathbf{P}}$ is defined as the total dipole moment per unit volume of the combined ionic and electronic subsystems,

$$\tilde{\mathbf{P}} = \frac{1}{\Omega}(\sum_{\alpha} Q_\alpha \mathbf{R}_\alpha - e\sum_{\beta} \mathbf{r}_\beta). \tag{1}$$

Here α runs over all the ion cores (that have a charge Q_α and are located at $\mathbf{R}_\alpha$) belonging to a selected unit cell; β runs over the Wannier centers (that possess a charge $-e$ and are located at $\mathbf{r}_\beta$) inside that unit cell; Ω is the supercell volume.

The total polarization could have been accessed more simply via the Berry-phase theory[25] in the Bloch representation, and indeed we checked that both methods yield same values (within numerical accuracy). However, the Wannier representation presents substantial advantages in the study of ferroelectric superlattices[26–28], in that it leads naturally to a *local* decomposition of $\tilde{\mathbf{P}}$ into the contribution of the individual perovskite layers,

$$\tilde{\mathbf{P}}_l = \frac{N}{\Omega}(\sum_{\alpha\in l} Q_\alpha \mathbf{R}_\alpha - e\sum_{\beta\in l} \mathbf{r}_\beta). \tag{2}$$

Here the sum is restricted only to the ion cores and Wannier centers that "belong" to the l-th perovskite cell (out of the N total cells) in the superlattice stack, in the sense specified in Ref. 30. Figure 1(a) displays the six different chosen unit cells for the case of the $[PTO]_3/[BFO]_3$ superlattice. Three of them, denoted by 1UC, 2UC and 3UC, contain a PbO and a TiO_2 layer each, i.e. they are made of pure $PbTiO_3$. The remaining three units are indicated as 4UC, 5UC and 6UC, and consist of pure $BiFeO_3$ layers.

Note that the individual units (1UC, ..., 6UC) do *not* possess inversion symmetry when taken separately, as they all consist of BO_2-AO couples. As a result, each unit can have a

nonzero dipole moment *even in the absence of a ferroelectric distortion*. In fact, the quantities $\tilde{\mathbf{P}}$ and $\tilde{\mathbf{P}}_l$ defined in Eq. (1) and (2) correspond to the so-called *formal* polarization[29]. This includes both the *effective* (i.e. ferroelectric) contribution, $\mathbf{P}$, and a *built-in* (non-switchable) polarization $\mathbf{P}^0$ that arises from the compositional (BO_2-AO) asymmetry of the individual unit cells. One can show that, within the conventions of Fig. 1, the built-in polarization is $P_z^0 = 0$ in PTO and $P_z^0 = +e/2a_{\rm IP}^2$ in BFO. Taking into account both contributions is particularly important at polar interfaces and charge-mismatched superlattices, where the use of the formal (total) $\tilde{\mathbf{P}}$ leads to a simple and elegant interpretation of the electrostatic coupling between layers[30].

Of course, these arguments only concern the polarization component along the stacking direction, $\tilde{P}_z$. Conversely, the in-plane components of $\mathbf{P}$ are irrelevant for the electrostatics – for simplicity, in the xy plane we shall always plot the effective $\mathbf{P}_\parallel = (P_x, P_y)$, by subtracting from the formal $\tilde{\mathbf{P}}_\parallel$ an appropriate fraction of the polarization quantum.

C. Other distortions

Finally, oxygen octahedra tilts (which are also commonly termed as antiferrodistortive motions) are decomposed too by unit cells in this study, according to the convention of Fig. 1b. Three of these unit cells are of $PbTiO_3$ type (those denoted by 1UC′, 2UC′, 3UC′) while the three others are constituted by BFO (those denoted by 4UC′, 5UC′ and 6UC′).

III. RESULTS AND DISCUSSION

Figures 2(a), (b) and (c) display the total energy of the equilibrium states, as well as their axial ratio, as a function of the in-plane lattice constant in films made of PTO, BFO and $[PTO]_3/[BFO]_3$, respectively (as all the three studied $[PTO]_n/[BFO]_n$ superlattices behave similarly, here we only show the results for $n = 3$). The in-plane lattice constant is varied between 3.54 Å and 4.27Å. Figures 3 display the x- and y-components of the effective polarization, the z-component of the formal (total) polarization, and all the Cartesian components of the *antiphase* antiferrodistortive (AAFD) vector as a function of $a_{\rm IP}$ in these equilibrium states for all the investigated materials. The inset of Figure 3(d) also shows the z-component of the *in-phase* antiferrodistortive (IAFD) vector. Note that our definitions of

the AAFD and IAFD vectors follow the usual convention: their axis is oriented along the direction about which the oxygen octahedra tilt, while their magnitude corresponds to the angle of such tilting[31]. In the following we shall first present the results for pure PTO and BFO films, in order to be able to appreciate and understand the physical properties of the epitaxial superlattices (to be discussed later).

A. Pure $PbTiO_3$ films

Figures 2(a) and 3 indicate that (001) epitaxial PTO films adopt four different ground states, depending on the value of $a_{\rm IP}$. These phases are: (1) a tetragonal $P4mm$ state, that only exhibits an effective polarization along the [001] growth direction ($\tilde{P}_z = P_z$ is shown with negative sign in Fig. 3(b) for reasons that will become clear later), for $a_{\rm IP}$ ranging between 3.59 Å and 3.91 Å – the energy minimum of this phase occurring at $a_{\rm IP} = a_{eq,PTO}$ =3.86 Å[32] [Note that Fig. 3(b) shows that, for this latter $a_{\rm IP}$, the effective polarization is predicted to be around 0.79 C/m^2, which is in excellent agreement with the measured value of 0.75 C/m^2 for single-crystals made of PTO bulk[33]]; (2) an orthorhombic $Ima2$ state, where an effective polarization lying along the [110] direction coexists with small antiphase tiltings of the oxygen octahedra (less than 2 degrees) about that same in-plane direction, for $a_{\rm IP}$ being larger than 3.91 Å but smaller than 4.09 Å. The energy minimum of this $Ima2$ phase occurs at $a_{\rm IP} = a_{Iam2,PTO}$ =3.93 Å; (3) a tetragonal $I4cm$ state that exhibits an out-of-plane component of both the effective polarization and AAFD vector for $a_{\rm IP}$ smaller than 3.59 Å; (4) an orthorhombic $Pmc2_1$ phase, where a large effective polarization lying along the in-plane [110] direction coexists with a small out-of-plane, in-phase tilting of the oxygen octahedra, for $a_{\rm IP} > 4.09\mathring{A}$. As depicted in Fig. 2(a), the axial ratio gradually increases from 0.85 to 1.42 when varying $a_{\rm IP}$ from 4.27 Å to 3.54 Å in PTO films. Note that the $I4cm$ state occurring at high compressive strain has never been reported before in epitaxial $PbTiO_3$ films to the best of our knowledge, unlike the P4mm and Ima2 phases[34,35]. Moreover, the $Pmc2_1$ state has just been recently discovered by us in $PbTiO_3$ (and also in $BiFeO_3$) systems under tensile strain[36]). It is worthwhile to know that this phase further possesses antiferroelectricity that is associated with the M-point of the 5-atom cubic Brillouin zone, therefore leading to inhomogenuous, zig-zag-like chains of cation displacement (see Ref.[36] for more details).

B. Pure $BiFeO_3$ films

Let us now concentrate on (001) BFO films. Consistent with previous theoretical works[36–38], we find that BFO films also adopt different ground states as $a_{\rm IP}$ decreases from 4.27 to 3.54 Å: (1) at small applied strain, the equilibrium state is a monoclinic Cc state (which is denoted here as Cc-I). This was indicated as the R-type phase in Ref.[1], as it bears close resemblance to the rhombohedral phase of bulk BFO. In particular, the effective polarization is roughly oriented along [111] and the AAFD vector is also close to that direction and rather large, e.g. it is around 14 degrees when $a_{\rm IP}$=$a_{eq,BFO}$ = 3.90$\mathring{A}$ – with $a_{eq,BFO}$ denoting the in-plane lattice parameter yielding the lowest possible total energy of BFO. When the strain is varied from moderately tensile to moderately compressive, both the effective polarization $\mathbf{P}$ and the AAFD vector rotate from the [110] towards the [001] directions in this Cc-I state. (2) For a compressive strain of 4.4% with respect to $a_{eq,BFO}$ (i.e., for $a_{\rm IP}$ = 3.73$\mathring{A}$), an isostructural, first-order transition occurs, which therefore generates another Cc state (indicated as Cc-II here, while being denoted as the T-like phase in Ref.[1]). This phase is characterized by a giant axial ratio and a large out-of-plane effective polarization. Cc-II also displays rather small x- and y-components of both the effective polarization $\mathbf{P}$ and the AAFD vector. These small components gradually decrease with decreasing $a_{\rm IP}$, and eventually vanish for $a_{\rm IP}$ smaller than 3.57 Å, where (3) a tetragonal, purely ferroelectric $P4mm$ state sets in. (4) For $a_{\rm IP}$ larger than 4.1 Å, the equilibrium state is the same phase as in PTO under large tensile strain, i.e. of $Pmc2_1$ symmetry. In BFO films, this state is characterized by a large in-plane effective polarization $\mathbf{P}_{\parallel}$, but also by a striking in-phase tilting of the oxygen octahedra (larger than 6 degrees) along the out-of-plane direction. The inhomogeneous cations movements associated with this $Pmc2_1$ state also lead to an orbital ordering between the d_{xz} and d_{yz} wavefunctions of the Fe ions[36].

It is important to stress that the formal polarization plotted in Fig. 3(b) is $\tilde{P}_z = P_z + P_z^0$; therefore, the ferroelectric polarization is given by the *difference* between the $\tilde{P}_z$ curve and the dashed $P_z^0 = e/2a_{\rm IP}^2$ curve. This difference is shown by a vertical arrow in Fig. 3(b). Our predicted values of z-component of the effective polarization are in good agreement with the corresponding values of ferroelectric polarization that are measured experimentally. For instance, for a_{IP} close to 3.81 Å, the computation gives P_z=0.68 C/m^2, while a recent measurement done on BFO films epitaxially grown on (La,Sr)(Al,Ta)O_3 (which corresponds

to a compressive strain of -2.4%) yielded a value of $\simeq 0.85$ C/m^2 for the z-component of the remanent polarization[39].

C. BFO/PTO superlattices

It is interesting to note that the global energy minima of BFO and PTO films occur at a similar value of $a_{\rm IP}$: $a_{eq,\rm BFO}$= 3.90 Å while $a_{eq,\rm PTO}$ = 3.86 Å. Such a small value of the misfit strain ($\simeq 1\%$) indicates that high-quality epitaxial growth of PTO/BFO superlattices should be experimentally possible. Another important observation concerns the behavior of the out-of-plane formal polarization in the superlattice. Because of the aforementioned difference in built-in polarization P_z^0 between the BFO and PTO layers, the electrostatic coupling between the two components is rather unusual in this system. We shall see in the following that these combined macroscopic effects (strain and charge), together with short-range interface effects (concerning the octahedral network) produces five different phases in $[\rm PTO]_3/[\rm BFO]_3$ within the range of investigated $a_{\rm IP}$[40]. As indicated in Figure 2(c), these are denoted as Phases I, I′, II, III and IV. Figures 4 further show the decomposition of the effective and formal polarization, as well as AAFD and IAFD vectors, in the different unit cells of the studied SL, to further characterize and understand important features of these five phases.

1. Phase I

This phase occurs for 3.87 Å $< a_{\rm IP} <$ 4.07 Å, a region of the phase diagram where pure BFO film is in a Cc-I phase (with the effective polarization vector approximately oriented along [111]), and pure PTO is in a $Ima2$ phase (with the effective polarization **P** being in plane). At first sight, these two phases appear electrostatically incompatible, since a significant out-of-plane component of the effective polarization is present in BFO (Cc-I), while $P_z = 0$ in PTO ($Ima2$). Typically, discontinuities in P_z along the z axis are forbidden because of the huge electric fields they would produce (with a large associated energy cost).

However, as we mentioned above, we must take into account the presence of a built-in compositional dipole in the BFO component of the SL. Once we sum up this *positive* contribution, $P_z^0 \sim 0.5$ C/m^2, with a *negative* ferroelectric polarization, $P_z \sim$ -0.5 C/m^2,

we obtain $\tilde{P}_z \sim 0$ in the BFO layers – as schematized in Fig. 1c; this is now perfectly compatible with the vanishing value of the formal (and thus effective) polarization of PTO films within this region of the phase diagram [Fig. 3(b)]. Thus, both components can preserve an electrical configuration that is very close to their respective pure-film ground state, as confirmed by the macroscopic (Fig. 3) and local (Fig. 4) analyses of $\tilde{P}_z$ and $\mathbf{P}_{\parallel}$ in the superlattice.

Interestingly, concerning the AAFD distortions of Phase I, Figures 3 and 4 show that there are significant differences with respect to the pure-film phases. For example, in the PTO component of the superlattice, small z-components of the AAFD vector (to be denoted as AAFD_z in the following) appear, while these are completely absent in the $Ima2$ phase of the pure PTO film; meanwhile, still in the PTO part, the x- and y-components of the AAFD vector (to be denoted as AAFD_{xy} in the following) are strongly enhanced compared to those in the pure PTO film at the same in-plane lattice constants. We interpret these as *proximity* effects, i.e. distortions that are locally induced near the interface by the presence of strong antiphase tiltings in the adjacent BFO part of the superlattice. In this context, the large enhancement in the AAFD_{xy} can be understood by our numerical finding (not shown here) that these modes are extremely soft in the $Ima2$ phase of PTO; the flatness of the potential energy landscape allows for large distortions at small energy cost.

2. Phase I′

At a larger compressive strain, corresponding to $a_{\mathrm{IP}} < 3.87$ Å, the AAFD_z distortions in the PTO layers undergo a sudden, drastic increase (see the local analysis in Fig. 4d). Meanwhile, for decreasing a_{IP}, $\tilde{P}_z$ adopts increasingly large negative values (see Fig. 3b), at the expense of the in-plane $\mathbf{P}_{\parallel}$, which progressively decreases in magnitude (see Fig. 3a). While the total polarization qualitatively follows the expected behavior (in both materials a compressive strain favors an out-of-plane component of the effective polarization $\mathbf{P}$ and eventually suppresses the in-plane component), the AAFD_z distortions in PTO layers constitute an original effect, which is absent in the pure PTO film (either in the $P4mm$ or $Ima2$ phases). Contrary to the Phase I discussed above, however, these enhanced AAFD_z are *not* a proximity effect, but rather a consequence of the mechanical *and* electrical boundary conditions experienced by the PTO component in the superlattice.

As a matter of fact, within the strain interval 3.77 Å $< a_{\rm IP} <$ 3.87 Å, which corresponds to a state of the SL denoted as Phase I′ hereafter, Figures 2a and 3b show that PTO would adopt a purely ferroelectric $P4mm$ phase, with a large value of -0.75 C/m^2 $< \tilde{P}_z < -1.0$ C/m^2 *in the absence of electrostatic constraints*. However, this is incompatible with $\tilde{P}_z$ in BFO, that in the same strain interval progressively decreases only from zero to -0.2 C/m^2 in the pure film (recall that this is the formal polarization – what is really happening is that the out-of-plane *ferroelectric* polarization is acquiring a progressively large negative value, from -0.5 C/m^2 to -0.8 C/m^2, in pure, compressed BFO films). In other words, in the superlattice, the BFO layer is opposing a strong resistance to the decrease of $\tilde{P}_z$ that is being promoted by the PTO component. As a consequence, $|P_z|$ in the PTO layer of the superlattice is significantly smaller with respect to that of the pure film – as evidenced in Figures 3b and 4b. This suppressed $|P_z|$ results in the occurrence of significant AAFD$_z$ rotations in the PTO layers in the Phase I′ of the SL, since it is well known that the AAFD distortions and the effective polarization *compete* in bulk PTO[35] (AAFD instabilities are present in the centrosymmetric reference phase, but disappear once the system relaxes to the ferroelectric ground state in bulk PTO). It is also interesting to realize that the transition from Phase I to Phase I′ is *isostructural* (since both phases adopt the same Pc space group) and is of second-order type (as emphasized by the energy curve displayed in Fig. 2c). Furthermore and as shown in the inset of Fig. 2(c), the monoclinic angle is smaller than 90 degrees only in the range of lattice constants defining Phase I′.

3. Phase II

Another phase occurs for 3.59 Å $< a_{\rm IP} <$ 3.77 Å. It is also monoclinic Pc, as Phases I and I′, implying that Phase I′ transforms into the present Phase II via another isostructural transition at an intermediate compressive strain of $\simeq$ -3.6%. This transition, however, is of first order, as evidenced by the jump in the axial ratio and monoclinic angle (see Figs. 2c and its inset), as well as in the AAFD and polarization vectors (cf Figs 3 and 4). Such features are similar to the strain-driven Cc-I–Cc-II phase transition occurring in (001) BFO films. Indeed, the local analysis of Fig. 4 shows that the BFO cells in the SL in Phase II have large out-of-plane component of the total polarization, significant in-plane components of both the effective polarization and AAFD vector, and negligible AAFD$_z$, exactly as in

the Cc-II state of BFO films. Note, however, that in the superlattice this transition occurs at slightly more moderate compressive strain values than in pure BFO films, as consistent with the tendency of PTO component to drive the system towards more negative values of $\tilde{P}_z$ (see discussion of Phase I′ above). This driving force produces a bias towards the Cc-II phase of BFO, which has a larger $|P_z|$ than the Cc-I phase – as evidenced by Fig. 3b. Note that the resulting $\tilde{P}_z$ in Phase II is still much less negative than $\tilde{P}_z$ in pure PTO at the same strain values. This explains why the AAFD_z distortions in the PTO layers of the SL are still large in this phase (see the discussion of the competition between AAFD and polarization in the Phase I′ above). Moreover, the in-plane components of the effective polarization $\mathbf{P}$ monotonically decrease for increasingly strong compressive strains, as expected; the local analysis shows that they are essentially vanishing in the PTO component.

4. Phase III

In close analogy with the second-order Cc-II–$P4mm$ transition in BFO films via the vanishing of the x- and y-components of both the effective polarization and AAFD vector, Phase II gradually transforms into Phase III at larger compressive strain in the SL – that is for a_{IP} smaller than 3.59 Å. Phase III has a tetragonal $P4bm$ space group. As indicated by Figs. 4, this phase is characterized by a giant out-of-plane formal polarization in the PTO and BFO cells and by significant AAFD_z tilts in the PTO cells (the AAFD vector is null in the BFO cells). Phase III can thus be simply considered as the superposition of the $P4mm$ state of pure BFO in the BFO cells with that of the $I4cm$ state of pure PTO in the PTO cells. However, this superposition is only "qualitative" rather than "quantitative". In fact, to enforce the continuity of $\tilde{P}_z$ across the superlattice, $|P_z|$ slightly increases (P_z becomes more negative in Fig. 3(b)) in the BFO cells (with respect to the pure film) and significantly decreases (P_z becomes less negative) in the PTO cells with respect to the pure-films cases. Once again, this suppressed $|P_z|$ in the PTO cells favors the AAFD_z tilts there, which in pure PTO films are much less pronounced.

5. Phase IV

Finally, another striking finding in the SL concerns the large tensile region, i.e. for $a_{\rm IP} > 4.07$ Å, where a new phase occurs. This latter phase is denoted as Phase IV and is also of Pc symmetry, which therefore implies that Phase III–Phase IV is the third isostructural transition exhibited by the superlattice! As revealed by Figs 2, 3 and 4, this transition is of first order. Phase IV resembles the $Pmc2_1$ state found in pure PTO and BFO films since it also exhibits (1) a large in-plane component of the effective polarization; (2) a vanishing AAFD vector; and (3) the activation of oxygen octahedra tilting *in-phase* about the z-axis, with the resulting tilting angle having a rather large magnitude (of the order of 4 degrees) near the transition, and further increasing with the tensile strain (see the inset of Fig. 3d). This large tilt mostly originates from the BFO cells, while the PTO cells also contribute more and more to it as $a_{\rm IP}$ increases – as shown by the inset of Fig. 4d. Interestingly, the $Pmc2_1$ states of pure PTO and BFO films are also characterized by a vanishing out-of-plane ferroelectric polarization, P_z, which make them electrostatically incompatible because of the compositional built-in P_z^0 (this P_z^0 is responsible for the discrepancy between upward- and left-oriented triangles at the right side of Fig. 3(b)). To neutralize this discontinuity, the PTO cells acquire a positive P_z, while the BFO cells acquire a *negative* ferroelectric P_z [see Fig. 4(b)] – therefore making $\tilde{P}_z$ homogeneous inside the superlattice. The $Pc - IV$ phase in the superlattice occurs at similar $a_{\rm IP}$ value as the transition to the $Pmc2_1$ state in either parent compound. Other properties of this region of the phase diagram accurately reflect the behavior of the parent compounds, which was detailed in Ref.[36]. It is however interesting to further know that, in the superlattice, the PTO layers do not exhibit any magnetism, unlike the BFO cells that possess a C-type ordering between their d_{yz} and d_{xz} orbitals. Therefore, Phase IV can be considered as an unique case of a system possessing a large (in-plane) effective polarization that propagates inside the whole SL (even if this polarization is inhomogeneous between the BFO and PTO layers, see Fig. 4a) coexisting with orbital ordering occurring only in one part of the SL.

6. Functional properties

Before closing, it is useful at this point to briefly discuss the functional properties of these superlattices, i.e. how the rich physics discussed in the above paragraphs manifests itself in an electrical (or electromechanical) measurement. One of the most important question regarding a ferroelectric superlattice is, of course, about the possibility to switch the polarization from a "down" to an "up" state and vice-versa. Note that switchability is far from obvious in the system discussed in the present work: The presence of the built-in compositional dipole introduces a strong violation of inversion symmetry, which typically biases the system towards a single electrical minimum[41]. To check this point we performed additional calculations at four selected values of the in-plane strain. Table I shows that a secondary minimum at a different total polarization value does exist in the intermediate to compressive region, while at large tensile strain values such a metastable state disappears. The absence of an oppositely polarized state at large tensile strain is not a surprise, as the out-of-plane component of the formal polarization within this region is of *dielectric* nature (the layers polarize to minimize the electrostatic mismatch between the components), not dissimilar to the situation in an insulating $LaAlO_3/SrTiO_3$ superlattice[30]. Conversely, the existence of the secondary minimum at the remaining three strain values is remarkable – we regard it as another consequence of the extraordinarily rich phase diagram of the constituent materials. Going into a detailed discussion would lead us outside the scopes of the present work; here, we limit ourselves to observing that, for $a_{\mathrm{IP}} = 3.81$ Å, the difference in energy between the two minima is as small as 50 meV per 60 atom, which indicates that both states are likely to be stable and useful for practical applications. Note that we also computed physical responses of the SLs, and found that in-plane dielectric and out-of-plane piezoelectric coefficients can be rather large (e.g., of the order of 120 and -10 C/m^2, respectively) for a_{IP} lattice constants associated with Phase I′, in general, and close to its border with Phase II, in particular. Such features are reminiscent of the significant physical responses found in pure BFO films in the Cc-I phase near the transition towards the Cc-II state[3,4,42].

IV. CONCLUSIONS

In summary, we used first-principles calculations to illustrate the existence of original features in short-period PTO/BFO superlattices. In particular, we described three isostructural transitions as a function of the in-plane lattice constant, two of first order and one of second order; the latter involves large anti-phase oxygen octahedra tiltings about the [001], out-of-plane direction in both BFO and PTO layers. Our simulations further pinpoint four ingredients to understand the properties of the investigated superlattices, namely, (1) the structural properties of the corresponding phases in the pure PTO and BFO films; (2) the distinction between effective (ferroelectric), built-in (non-switchable) and formal (total) polarization and the continuity of the latter; and (3) the competitive interaction between polarization and oxygen octahedral tilting. We therefore hope that this present work will be of large benefit to the active research fields of phase transitions, nanoscience, ferroelectrics and multiferroics.

Acknowledgments

This work is mostly supported by the Department of Energy, Office of Basic Energy Sciences, under contract ER-46612. We also acknowledge NSF grants DMR-1066158 and DMR-0701558, ARO Grant W911NF-12-1-0085 and ONR Grants N00014-11-1-0384 and N00014-08-1-0915. M. S. acknowledges support by DGI-Spain through Grants No. MAT2010-18113 and No. CSD2007-00041, and by the European Union through the project EC-FP7, Grant No. NMP3-SL-2009-228989 "OxIDes". W. R. acknowledges the Eastern Scholar Professorship at Shanghai Institutions of Higher Education, Shanghai Municipal Education Commission, and the support from National Natural Science Foundation of China under Grant No. 11274222. Some computations were also made possible thanks to the MRI grant 0722625 from NSF, the ONR grant N00014-07-1-0825 (DURIP) and a Challenge grant from the Department of Defense.

[1] R. J. Zeches, M. D. Rossell, J. X. Zhang, *et al.*, *Science* **326**, 977 (2009).

[2] H. Béa, B. Dupé, S. Fusil, et al., *Phys. Rev. Lett.* **102**, 217603 (2009).

[3] J. C. Wojdeł and J. Íñiguez, *Phys. Rev. Lett.* **105**, 037208 (2010).

[4] S. Prosandeev, I. A. Kornev, and L. Bellaiche, *Phys. Rev. B* **83**, 020102 (2011).

[5] S. Y. Yang, J. Seidel, S. J. Byrnes, *et al.*, *Nature Nano.* **5**, 143 (2010).

[6] J. Seidel, D. Fu, S.-Y. Yang, *et al.*, *Phys. Rev. Lett.* **107**, 126805 (2011).

[7] I. C. Infante, S. Lisenkov, B. Dupé, *et al.*, *Phys. Rev. Lett.* **105**, 057601 (2010).

[8] I. C. Infante, J. Juraszek, S. Fusil, *et al.*, *Phys. Rev. Lett.* **107**, 237601 (2011).

[9] K.-T. Ko, M. H. Jung, Q. He, *et al.*, *Nature Commun.* **2**, 567 (2011).

[10] S. Prosandeev, I. A. Kornev, and L. Bellaiche, *Phys. Rev. Lett.* **107**, 117602 (2011).

[11] Y. W. Li, Y. D. Shen, F. Y. Yue, *et al.*, *J. Cryst. Growth* **312**, 617 (2010).

[12] R. Ranjith, W. Prellier, J. W. Cheah, *et al.*, *Appl. Phys. Lett.* **92**, 232905 (2008).

[13] L. Pálová, P. Chandra, and K. M. Rabe, *Phys. Rev. Lett.* **104**, 037202 (2010).

[14] A. Y. Borisevich, H. J. Chang, M. Huijben, *et al.*, *Phys. Rev. Lett.* **105**, 087204 (2010).

[15] A. Ohtomo and H. Y. Hwang, *Nature* **427**, 423 (2004).

[16] N. Reyren, S. Thiel, A. D. Caviglia, *et al.*, *Science* **317**, 1196 (2007).

[17] S. Valencia, A. Crassous, L. Bocher, *et al.*, *Nature Mater.* **10**, 753 (2011).

[18] E. Bousquet, M. Dawber, N. Stucki, *et al.*, *Nature* **452**, 732 (2008).

[19] I. A. Vladimir, F. Aryasetiawan, and A. I. Lichtenstein, *J. Phys: Condens. Mat.* **9**, 767 (1997).

[20] I. A. Kornev, S. Lisenkov, R. Haumont, B. Dkhil, and L. Bellaiche, *Phys. Rev. Lett.* **99**, 227602 (2007).

[21] G. Kresse and D. Joubert, *Phys. Rev. B* **59**, 1758 (1999).

[22] H. Béa, M. Bibes, A. Barthelemy, *et al.*, *Appl. Phys. Lett.* **87**, 072508 (2005).

[23] See http://www.cryst.ehu.es/cryst/bplot.html. And see http://stokes.byu.edu/findsym.html.

[24] A. A. Mostofi, J. R. Yates, Y.-S. Lee, *et al.*, *Comput. Phys. Commun.* **178**, 685 (2008).

[25] R. D. King-Smith and D. Vanderbilt, *Phys. Rev. B* **47**, 1651 (1993).

[26] E. D. Murray and David Vanderbilt, *Phys. Rev. B* **79**, 100102(R) (2009).

[27] X. Wu, O. Diéguez, K. M. Rabe, and D. Vanderbilt, *Phys. Rev. Lett.* **97**, 107602 (2006).

[28] M. Stengel and N.A. Spaldin, *Phys. Rev. B* **73**, 075121 (2006).

[29] R. Resta and D. Vanderbilt, Physics of Ferroelectrics: A Modern Perspective, editors K. M. Rabe and C. H. Ahn and J.-M. Triscone (Springer-Verlag, Berlin Heidelberg, 2007)

[30] M. Stengel and D. Vanderbilt, *Phys. Rev. B* **80**, 241103 (2009).

[31] A. Glazer, *Acta Crystallogr., Sect. B* **28**, 3384 (1972).

[32] Note that our theoretical lattice constants are underestimated by roughly 1-2 % with respect to measurements due to the use of the LSDA scheme.

[33] Li Sun, Yan-Feng Chen, Wei-Hui Ma, *et al*, *Appl. Phys. Lett.* **68**, 3728 (1996).

[34] C. Bungaro and K. M. Rabe, *Phys. Rev. B* **69**, 184101 (2004).

[35] J. L. Blok, D. H. A. Blank, G. Rijnders, K. M. Rabe, and D. Vanderbilt, *Phys. Rev. B* **84**, 205413 (2011).

[36] Y. Yang, W. Ren, M. Stengel, X. H. Yan, L. Bellaiche, *Phys. Rev. Lett*, **109**, 057602 (2012).

[37] A. J. Hatt, N. A. Spaldin, and C. Ederer, *Phys. Rev. B* **81**, 054109 (2010).

[38] B. Dupé, S. Prosandeev, G. Geneste, B. Dkhil, and L. Bellaiche, *Phys. Rev. Lett.* **106**, 237601 (2011).

[39] C. Daumont, W. Ren, I. C. Infante, *et al*, *J. Phys.: Condens. Matter* **24**, 162202 (2012).

[40] These five phases also occur in $[PTO]_1/[BFO]_1$ and $[PTO]_2/[BFO]_2$ superlattices.

[41] H. Das, N.A. Spaldin, U.V. Waghmare and T. Saha-Dasgupta, *Phys. Rev. B* **81**, 235112 (2010).

[42] Z. Chen, S. Prosandeev, Z. Luo, *et al*, *Phys. Rev. B* **84**, 094116 (2011).

TABLE I: z-component of the formal polarization ($\tilde{P}_z$), and of the effective polarization in PTO and BFO cells ($P_{z,PTO}$, $P_{z,BFO}$) for the lowest-in-energy state and the metastable state with opposite direction of the polarization in the $[PTO]_3/[BFO]_3$ superlattice, at four selected in-plane lattice constants. The energy difference between these two states is shown in the last column, and is given in meV per 60 atom. The lattice constant and polarizations are given in $\mathring{A}$ and C/m^2, respectively

a_{IP} (corresponding Phase)	Lowest-in-energy			Metastable state			ΔE
	$\tilde{P}_z$	$P_{z,PTO}$	$P_{z,BFO}$	$\tilde{P}_z$	$P_{z,PTO}$	$P_{z,BFO}$	
3.69 (II)	-0.949	-0.949	-1.537	1.350	1.350	0.763	546
3.81 (I′)	-0.245	-0.245	-0.796	1.037	1.037	0.486	50
3.90 (I)	-0.022	-0.022	-0.548	0.830	0.830	0.304	381
4.16 (IV)	0.155	0.155	-0.307	N/A	N/A	N/A	N/A

FIGURE CAPTIONS

Figure 1: (Color online) Features of the studied epitaxial (001) $[PTO]_3/[BFO]_3$ superlattice film. Panel (a) represents the atomic arrangement of this system, as well as, the six cells involved in the definition of the local polarization (see Eq. (2)). Panel (b) displays the six cells that are used to extract the cell-by-cell decomposition of antiferrodistortive motions. Panel (c) shows a schematic of the z-component of the effective ($\mathbf{P}$), built-in ($\mathbf{P}^0$) and formal ($\tilde{\mathbf{P}}$) polarizations in the BFO and PTO cells. Blue arrow express the built-in polarization and orange arrow express the effective polarization.

Figure 2: (Color online) Total energy (left vertical axis) and axial ratio (right vertical axis) as a function of the in-plane lattice parameter for the equilibrium phases in epitaxial (001) PTO films (Panel a), BFO films (Panel b) and in the $[PTO]_3/[BFO]_3$ superlattices (Panel c). The inset of Panel (c) displays the monoclinic angle of the $[PTO]_3/[BFO]_3$ superlattice.

Figure 3: (Color online) Properties of epitaxial (001) PTO, BFO and $[PTO]_3/[BFO]_3$ films versus the in-plane lattice parameter in the equilibrium phases. Panels (a) and (b) show the x-component (which is identical to its y-component) of the effective polarization and the z-component of the formal polarization, respectively. Panels (c) and (d) display the x-component (which is identical to its y-component) and the z-component of the AAFD vector (see text), respectively. The inset of Panel (d) represents the angle made by oxygen octahedra tilting *in-phase* about the z-axis, θ_z. In Panel (b), the effective polarizations of BFO and PTO films are shown by means of vertical arrows.

Figure 4: (Color online) Predicted local properties of epitaxial (001) $[PTO]_3/[BFO]_3$ superlattice versus the in-plane lattice parameter in the equilibrium phases. Panels (a) and (b) show the x-component (which is identical to its y-component) of the local effective polarization and the z-component of the local formal polarization in the six cells indicated in Fig. 1a, respectively. Panels (c) and (d) display the x-component (which is identical to its y-component) and the z-component of the cell-by-cell decomposition of the AAFD vector in the six cells displayed in Fig. 1b, respectively. The inset of Panel (d) represents the in-phase

octahedra tilting in the six cells shown in Fig. 1b. In Panel (b), the effective polarizations of BFO and PTO cells are shown by means of vertical arrows.

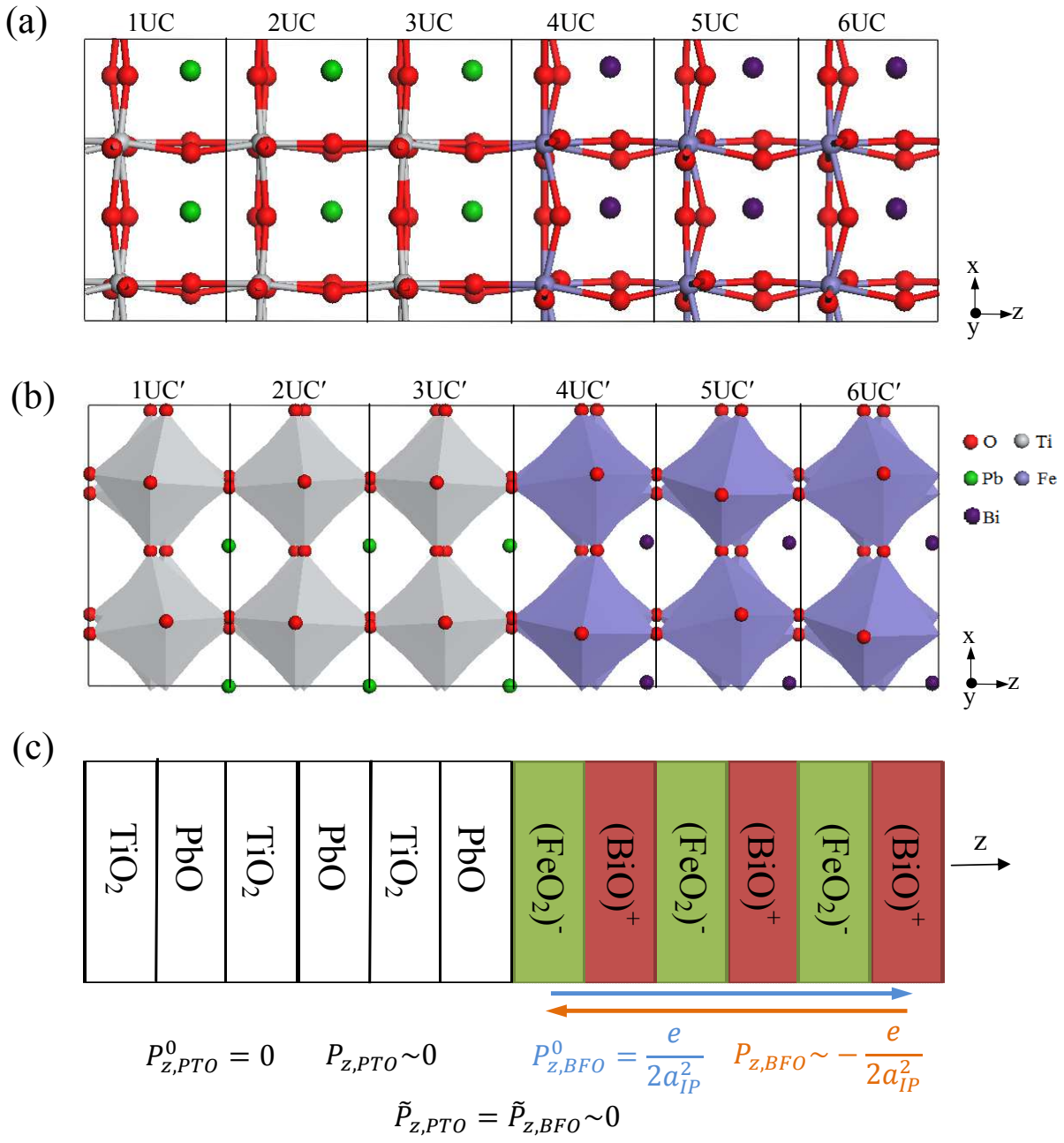

Figure 1 BV11658 05Oct2012

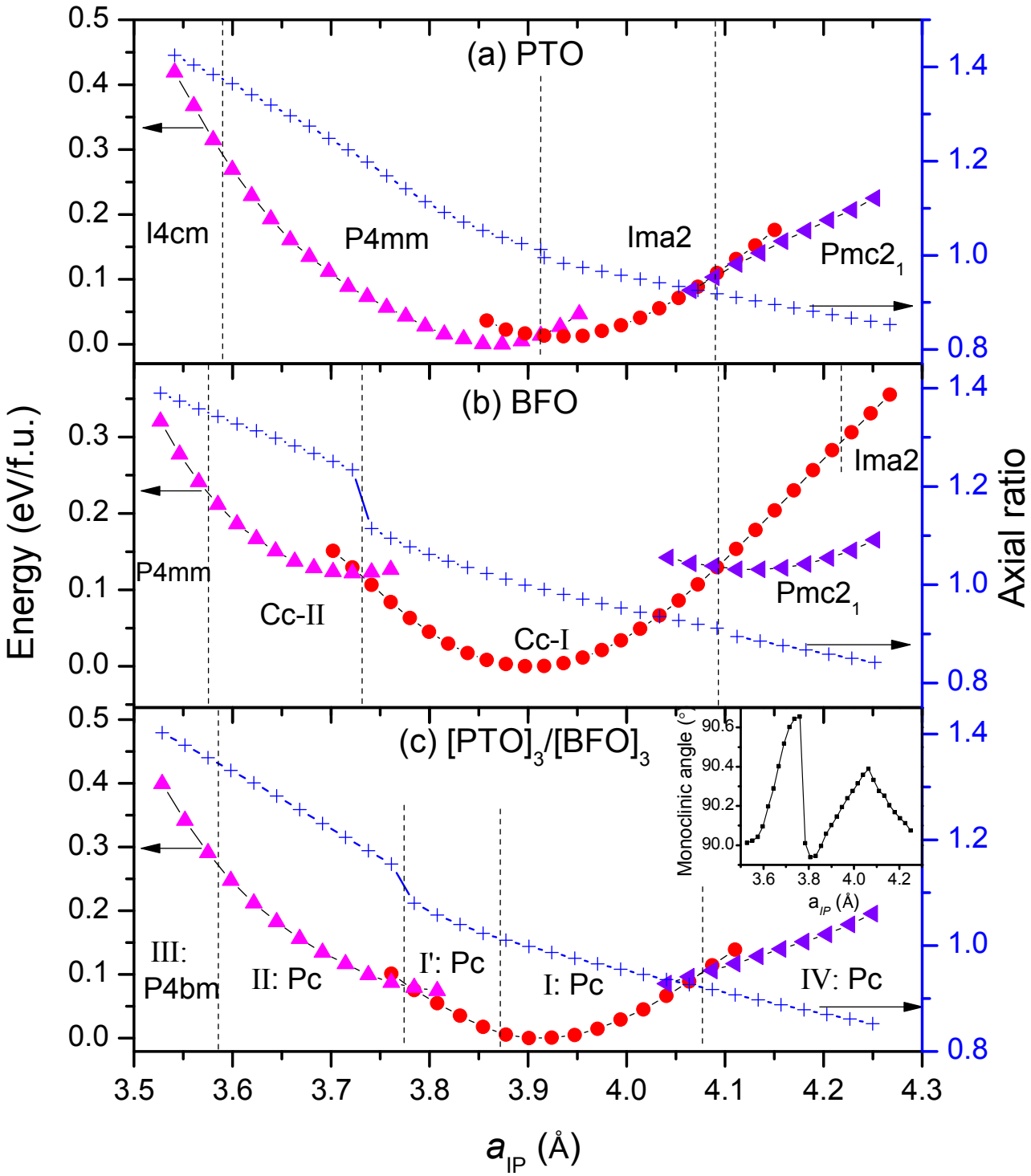

Figure 2 BV11658 05Oct2012

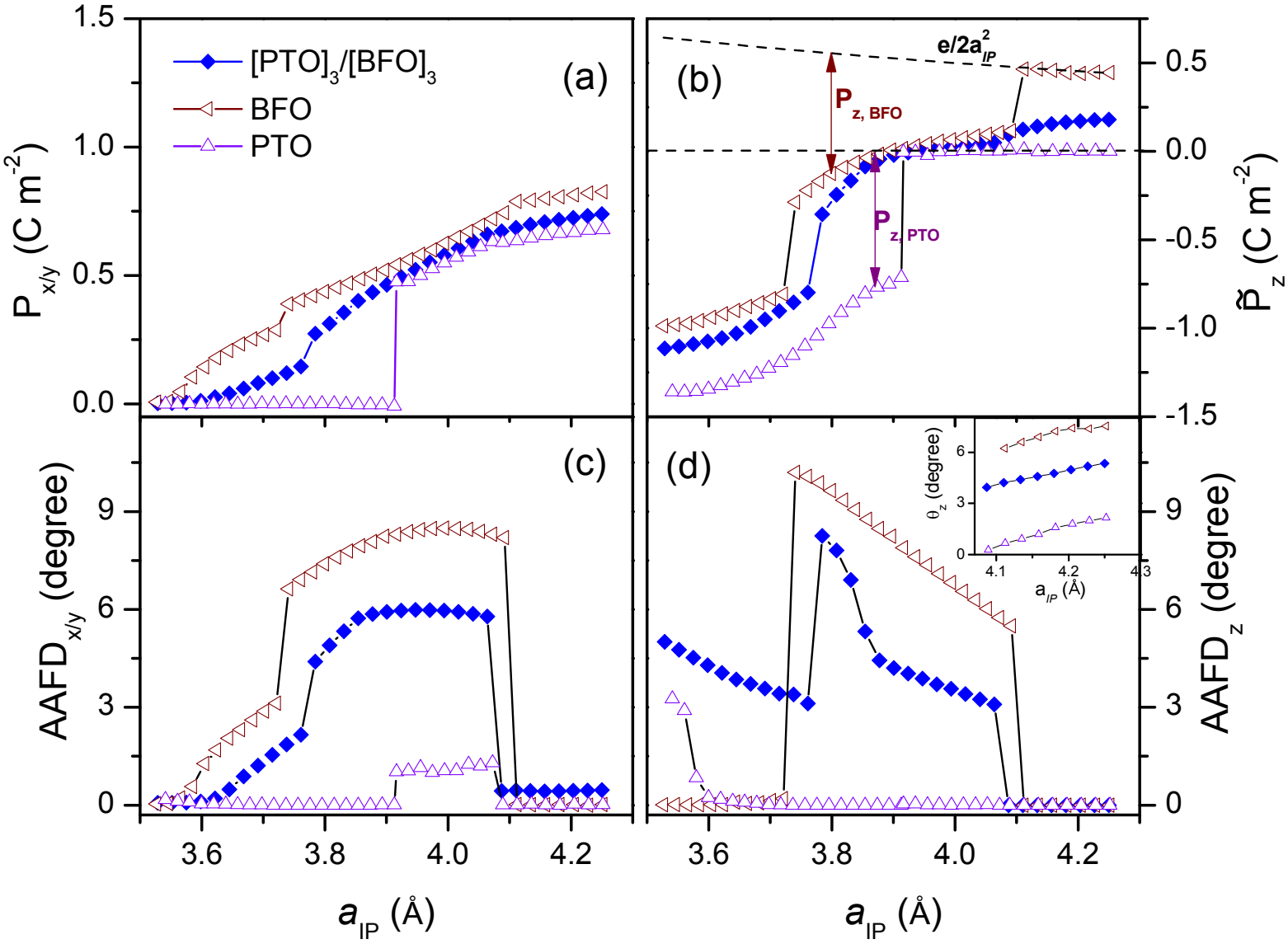

Figure 3 BV11658 05Oct2012

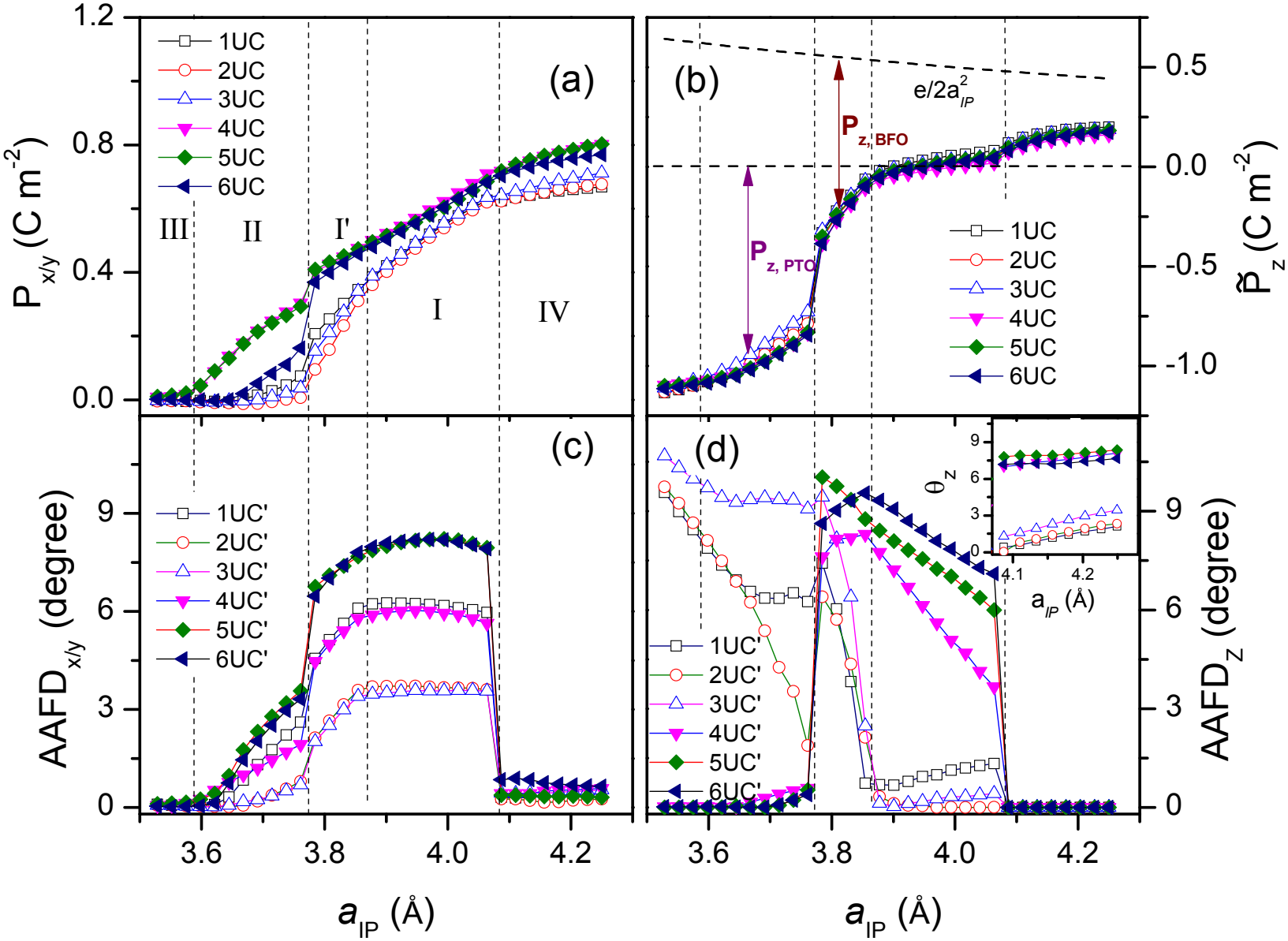

Figure 4 BV11658 05Oct2012